Chemical Engineering Science 66 (2011) 3452–3458

Contents lists available at ScienceDirect

Chemical Engineering Science

journal homepage: www.elsevier.com/locate/ces

Contact line motion without slip in lattice Boltzmann simulations

M.R. Kamali [a,*], J.J.J. Gillissen [a], S. Sundaresan [b], H.E.A. Van den Akker [a]

[a] Department of Multi-Scale Physics, Delft University of Technology, Delft, Netherlands
[b] Department of Chemical Engineering, Princeton University, Princeton, NJ 08544, USA

ARTICLE INFO

Article history:
Received 28 October 2010
Received in revised form
7 April 2011
Accepted 10 April 2011
Available online 28 April 2011

Keywords:
Lattice Boltzmann method
Segmented bubble flow
Multi-phase flow
Contact angle dynamics
Partially wetting
Capillary

ABSTRACT

We have simulated the pressure driven motion of a gas bubble immersed in a partially wetting liquid in a two-dimensional channel using the Shan and Chen multi-phase lattice Boltzmann (LB) method. Both the one-component and the two-component multi-phase models of the Shan–Chen approach have been used. The static contact angle at the fluid–solid interface was controlled by adjusting the fluid–solid interaction potential. The variation of the dynamic contact angle with the capillary number obtained from the LB simulations was compared with experimental data from the literature. Our results indicate that in the LB simulation the contact line moves over the no-slip surface due to evaporation at the nose and condensation at the tail of the bubble. This is in contrast to reality where slip at the contact line facilitates the bubble motion. We show that by controlling the extent of phase transition the simulations can be brought into close agreement with experimental data from the literature.

1. Introduction

Wetting phenomena are not only an inseparable part of nature but also play an important role in many industrial processes which involve fluid interaction with solid surfaces. Examples of such processes are chemical reactors involving the flow of gaseous and liquid-phase reactants over a catalyst deposited on a solid wall or solid particles, such as in trickle-bed reactors, fixed-bed reactors and so on (Vervloet et al., 2009; Tsamatsoulis and Papayannakos, 1996; Lunkad et al., 2007). Such reactors are best described by means of multi-scale models (Van Den Akker, 2010) in which processes at the micro-scale and at the reactor scale affect one another. A proper understanding and computational simulation of the micro-scale processes may therefore be indispensable for simulating and improving reactor performance (Vervloet et al., 2009; Lerou and Ng, 1996). In this paper, we will focus on the motion of a gas–liquid–solid contact line as an important issue (at the micro-scale) in a three-phase partially wetted chemical reactor.

In partially wetting two-phase systems, the fluid–wall interaction prohibits both fluids from fully wetting the available solid surfaces. This gives rise to contact lines at the fluid–fluid–wall intersection. In such a case, the contact angle defined as the angle between the fluid–fluid interface and the solid surface at the three-phase contact line is non-zero. Partially wetting phenomena have mainly been studied in static cases where the contact angle barely deviates from its equilibrium value. However, the dynamic behaviour of contact lines is crucial in many applications. In spite of many experimental and theoretical studies (Cox, 1986a,b; Hoffman, 1975; Jiang et al., 1979; Ralston et al., 2008), the dynamics of the moving contact line and the associated dynamic contact angle are still not well understood. This is due to the interplay of phenomena occurring over a wide range of length scales ranging from the bubble size down to the intermolecular distance.

There are two main classes of models which are used to describe contact line dynamics. In molecular dynamics (MD) simulations, one computes the motion of many individual molecules and their interactions (Koplik et al., 1988, 1989). By averaging the MD one can obtain the macroscopic fluid behaviour. MD provide a means for explicitly studying the influence of the solid surface properties and the wall–fluid interactions. In spite of its advantages, MD is an expensive and computationally demanding method for complex geometries (Ralston et al., 2008; Zhang, 2011).

The other approach starts from the macroscopic fluid equations and has mainly been used to concentrate on the viscous deformation of the interface next to the wall. In this hydrodynamical approach, one has to resort to models in order to resolve the phenomena within the intermolecular distance to the contact line. The hydrodynamic description of the moving contact line requires a violation of the no-slip boundary condition in order to alleviate an otherwise infinite shear stress at the contact line that would prohibit the bubble from moving (Ralston et al., 2008).

In order to avoid this stress singularity, alternative conditions have been proposed. These conditions involve a parameter referred to as the slip length l_s, which is of the order of the intermolecular

* Corresponding author. Tel.: +31 15 27 83252; fax: +31 15 27 82838.
E-mail addresses: M.R.Kamali@tudelft.nl, mdrzkamali@gmail.com (M.R. Kamali).

0009-2509/$ - see front matter © 2011 Elsevier Ltd. All rights reserved.
doi:10.1016/j.ces.2011.04.010

distance. By relaxing the no-slip boundary condition, the force exerted on the solid wall in the vicinity of the three-phase contact line will remain finite. By using such a type of boundary condition one can solve the Navier–Stokes equations and obtain a relation for the dynamic contact angle versus the bubble velocity.

Cox (1986a) derived a generalized analytical solution for the case of a moving interface on a smooth solid wall by using the method of matched asymptotic expansions. In its simplest form, Cox's equation can be written as

$$\theta^3-\theta_0^3=\frac{Ca}{Ca^*}, \tag{1}$$

which is known as Cox–Voinov equation (Cox, 1986a; Voinov, 1977). Eq. (1) describes the change in the dynamic contact angle θ as a function of the static contact angle θ_0 and the capillary number Ca:

$$Ca=\frac{\mu_{liq}U}{\sigma}, \tag{2}$$

where σ is the fluid–fluid surface tension, μ_{liq} is the liquid dynamic viscosity and U is the bubble velocity. The model parameter Ca^* in Eq. (1) is referred to as the typical capillary number which depends on l_s/R and can be interpreted of as the mobility of the contact line.

The relation between Ca^* and l_s/R was numerically studied by Sheng and Zhou (1992) for the case of a gas–liquid interface in a channel by using different slip models. They used a computational grid which resolved all scales ranging from the channel radius R down to the slip length l_s.

Numerical simulations of dynamic contact angles using slip length models such as Sheng and Zhou (1992) require resolving all length scales ranging from the macroscopic geometry down to the slip length, which is of the order of the intermolecular distance. Therefore the application of these models has been limited to simple problems (Ralston et al., 2008).

In more complex problems, a full resolution of the intermolecular length scales at the contact lines are infeasible and one has to resort to ad hoc modelling, such as a prescribed contact angle as a function of the contact line speed (see for instance Spelt, 2005).

In the present work we will investigate the potential of the lattice Boltzmann method as an alternative route to simulate contact line dynamics. The lattice Boltzmann (LB) method is a mesoscopic approach which lies in between MD and conventional (finite volume) computational fluid dynamics (CFD). In the LB method, a fluid is represented by a set of fictitious particles exhibiting discrete velocities in specific directions. In the macroscopic, incompressible limit, the LB method recovers the Navier–Stokes equations (Succi, 2001). In general, the LB method has several advantages over the conventional finite volume technique of CFD. For a concise review of the LB method and its pros and cons for engineering applications, the reader is referred to Raabe (2004), Van Den Akker (2010) and Akker (2006).

When simulating contact line dynamics, the LB method provides multiple (additional) advantages. Particularly, we do not need to track the evolution of the fluid–fluid interface, while this is essential and computationally expensive in such methods as the volume of fluid, the level-set and the front-tracking methods. In addition, compared to macroscopic models and simulations, it is relatively easy to incorporate intermolecular interactions between a fluid and a solid surface without increasing the computational costs (Zhang, 2011; Aidun and Clausen, 2010). As two fluid phases (the gas and the liquid) are involved, a short introduction to two-phase LB methods is given first.

There are different LB based multi-phase models. Some of those have been used for studying contact line motion with some degree of success (Briant et al., 2004; Fan et al., 2001; Grubert and Yeomans, 1999; Harting et al., 2010; Hyväluoma et al., 2007; Sbragaglia et al., 2008). In the current paper, we use the pseudo-potential, one-component and two-component methods of Shan and Chen (1993) with a view to simulate the pressure driven flow of a bubble in a partially wetting liquid in a two-dimensional channel. The main focus will be on the viscous deformation of the gas–liquid interface, quantified by the dynamic contact angle as a function of the velocity of the interface, expressed in terms of the capillary number Ca (Eq. (2)). In addition to Ca, the dynamic contact angle is further determined by the viscosity ratio between the two fluids and the static contact angle (Cox, 1986a; Sheng and Zhou, 1992; Voinov, 1977). Previous work showed that for a viscosity ratio of one (liquid–liquid) the Shan–Chen model predicts a dynamic contact angle in close agreement with experimental data (Fan et al., 2001).

In the present investigation, we apply the LB method for viscosity ratios which resemble a gas–liquid system. In this contribution, we will argue that evaporation and condensation at the nose and the tail of the moving bubble is the mechanism that facilitates the motion of the three-phase contact line in the Shan-Chen LB approach. We will demonstrate that by controlling the amount of evaporation and condensation the simulations can be brought into close agreement with the experimental data of Hoffman (1975).

2. Numerical method

Our numerical method is based on the pseudo-potential, multi-component, lattice Boltzmann (LB) method of Shan and Chen (1993). In this method, the flow of multiple components is simulated. The different components are treated as inter-penetrable continua which are represented by separate hydrodynamic fields. The different fields are assigned different values for the index $\delta\in\{1,\ldots,N\}$. The different components obey non-ideal equations of state which can separate them into different phases having different densities.

With the Shan–Chen model multi-phase flow can be simulated using a single component or multiple components. In one-component multi-phase flow simulations the two phases have a large degree of miscibility, due to phase transition at the gas–liquid interface. Immiscibility can be improved by using two components instead of one, such that each component occupies one of the two phases with a large degree of purity.

Here we discuss the details of the method for the general case of N components. The method solves the discretized version of the Boltzmann equation, describing the evolution of the particle distribution function of each component $f^\delta(\boldsymbol{v},\boldsymbol{x},t)$ in the space, spanned by the particle velocity $\boldsymbol{v}$ and the particle position $\boldsymbol{x}$ (Succi, 2001). By taking moments of the Boltzmann equation one recovers the conservation equations for the macroscopic flow properties such as the densities of mass, momentum and energy (Succi, 2001). Multi-phase flow behaviour and phase separation is obtained by incorporating microscopic interactions between fluid particles through non-ideal equations of state. Furthermore, interfacial tension σ is automatically captured by introducing attractive/repulsive forces between neighbouring fluid elements.

In the present lattice Boltzmann method, the position space is discretized on a homogeneous and square lattice with a grid spacing of Δx and the velocity-space is projected onto a discrete set of velocities $\boldsymbol{v}_\alpha$. These discrete velocities are matched to the underlying spatial lattice, such that $\boldsymbol{v}_\alpha\Delta t=(a,b,c)_\alpha\Delta x$, where Δt is the computational time step and a, b and c attain values of $\{-1,0,1\}$.

The probability distribution function of each component δ is discretized into nine components f_α^δ, corresponding to nine velocity directions $\boldsymbol{v}_\alpha$. In the literature this velocity lattice is referred to as D2Q9. Fluid mass density ρ^δ and momentum density $\rho^\delta \boldsymbol{u}^\delta$ are related to f_α^δ through:

$$\rho^\delta = \sum_\alpha f_\alpha^\delta, \tag{3a}$$

$$\rho^\delta \boldsymbol{u}^\delta = \sum_\alpha f_\alpha^\delta \boldsymbol{v}_\alpha. \tag{3b}$$

The evolution equations for f_α^δ describe a relaxation process towards the truncated Maxwell–Boltzmann distribution $f_\alpha^{eq,\delta}$ (Succi, 2001; Shan and Chen, 1993):

$$f_\alpha^\delta(\boldsymbol{x}+\boldsymbol{v}_\alpha\Delta t, t+\Delta t) = (1-(\tau^\delta)^{-1}) f_\alpha^\delta(\boldsymbol{x},t) + (\tau^\delta)^{-1} f_\alpha^{eq,\delta}(\boldsymbol{x},t), \tag{4}$$

where the relaxation time τ^δ is related to the kinematic viscosity v^δ as $\tau^\delta = \Delta t(\frac{1}{2} + 3v^\delta \Delta t/\Delta x^2)$. In all the simulations reported in this paper we have used $\tau^\delta = 1\Delta t$ corresponding to $v^\delta = \frac{1}{6}\Delta x^2/\Delta t$ for $\delta = 1,2$.

It is noted that in the present method the kinematic viscosity v^δ is constant. When dealing with multi-phase flow, the method permits sharp density variations, such that liquid-like and gas-like regions coexist, each having different values of the dynamic viscosity.

The Maxwell–Boltzmann distribution $f_\alpha^{eq,\delta}$ is given by (Succi, 2001; Shan and Chen, 1993)

$$f_\alpha^{eq,\delta}(\boldsymbol{x},t) = w_\alpha \rho^\delta(\boldsymbol{x}) \left[1 + \frac{\tilde{\boldsymbol{u}}^\delta \cdot v_\alpha}{c_s^2} + \frac{1}{2}\frac{(\tilde{\boldsymbol{u}}^\delta \cdot v_\alpha)^2}{c_s^4} - \frac{1}{2}\tilde{\boldsymbol{u}}^\delta \cdot \frac{\tilde{u}^\delta}{c_s^2} \right]. \tag{5}$$

Here $c_s = 3^{-1/2}\Delta x/\Delta t$ is the speed of sound and w_α are the quadrature weights corresponding to the projection of f^δ onto the D2Q9 lattice. By basing $f_\alpha^{eq,\delta}$ on the modified velocity:

$$\tilde{\boldsymbol{u}}^\delta = \boldsymbol{u}' + \tau^\delta \boldsymbol{F}/\rho^\delta \tag{6}$$

in which the macroscopic velocity $\boldsymbol{u}'$ is defined as

$$\boldsymbol{u}' = \frac{\sum_\delta \rho^\delta \boldsymbol{u}\delta/\tau^\delta}{\sum_\delta \rho^\delta/\tau^\delta} \tag{7}$$

the model accounts for a total body force $\boldsymbol{F} = \boldsymbol{F}^\delta + \boldsymbol{F}^{\mathbf{ext}}$, which constitutes both external body forces $\boldsymbol{F}^{\mathbf{ext}}$ such as gravity and pressure gradient as well as the mean field intermolecular interaction forces $\boldsymbol{F}^\delta$ between particles. The mean field force includes both fluid–fluid and fluid–solid interactions and is generally defined as a low order approximation of $\Psi^\delta \sum_{\bar\delta} \nabla \Psi^{\bar\delta}$, where Ψ^δ is referred to as the pseudo-potential or effective density (Shan and Chen, 1993).

$$\boldsymbol{F}^\delta = \frac{-1}{\Delta t}\Psi^\delta(\boldsymbol{x}) \sum_{\bar\delta=1}^{N} G^{\delta\bar\delta} \sum_\alpha w_\alpha \Psi^{\bar\delta}(\boldsymbol{x}+\Delta t \boldsymbol{v}_\alpha)\boldsymbol{v}_\alpha. \tag{8}$$

The force potential Ψ^δ is a monotonically increasing function of the density ρ^δ which determines the non-ideal fluid behaviour. The values for $G^{\delta\bar\delta}$ determine the equilibrium densities of the phases, the level of immiscibility between the different phases, the sharpness of interface and the surface tension. To explain the influence of these parameters we consider the case where number of components $N=2$ and assume that $\delta = 1$ and 2 correspond to a liquid-like component and a gas-like component, respectively. A negative G^{11} corresponds to attractive forces between the liquid molecules and a positive $G^{12} = G^{21}$ corresponds to repulsive forces between the gas and the liquid molecules. Usually an ideal gas will be recovered by using $G^{22} = 0$.

Originally, the Shan and Chen multi-phase flow model was limited to a rather low density ratio between the different phases $D = \rho^{liq}/\rho^{gas}$ due to numerical instabilities and large parasitic velocities along the interface (Shan, 2006). As was proposed by Yuan and Schaefer (2006), it is possible to increase this density ratio by tuning the pseudo-potential Ψ^δ in Eq. (8). By properly choosing the dependence of Ψ^δ on ρ^δ, one can in principle recover any desired, non-ideal equation of state (EOS) $p^\delta(\rho^\delta)$ and increase D accordingly.

$$\Psi^\delta = \sqrt{2\left(\frac{p^\delta(\rho^\delta)}{c_s^2} - \rho^\delta\right)}. \tag{9}$$

Even though the method proposed by Yuan and Shaefer is based on a single component we can also use it for a two-component systems by allowing each component to obey its own EOS through a separate $\Psi^\delta(\rho^\delta)$. In this work we follow such an approach and achieve large density ratios in both one- and a two-component multi-phase systems.

In our one-component simulations we use the Carnahan–Starling equation of state (EOS) (Yuan and Schaefer, 2006; Carnahan and Starling, 1970a,b):

$$\frac{p}{\rho_0^\delta c_s^2} = a\tilde{\rho^\delta}\left[\frac{1+\tilde{\rho^\delta}+(\tilde{\rho^\delta})^2-(\tilde{\rho^\delta})^3}{(1-\tilde{\rho^\delta})^3}\right] - b(\tilde{\rho^\delta})^2, \tag{10}$$

while in our two-component simulations we use Eq. (10) for the liquid-like component ($\delta = 1$) and we use the ideal gas EOS $\Psi^\delta = \rho^\delta$ for the gas-like component ($\delta = 2$).

In Eq. (10) $\tilde{\rho^\delta} = \rho^\delta/\rho_0^\delta$ is a non-dimensional density with respect to the reference density ρ_0^δ and a and b denote two non-dimensional parameters, which are linked to the temperature T and the intermolecular forces. In the simulations we use $b=3$. For this particular choice there is a convenient interpretation of parameter a as $a = 0.28T_R$, where the reduced temperature $T_R = T/T_C$ is the ratio of the temperature T to the critical temperature T_C. By adjusting a we could control the extent of phase separation and the accompanying density ratio D and the surface tension σ.

The present numerical method is designed to deal with flows over solid walls. The walls impose a no-slip condition, to the fluid. Assuming the solid walls to be parallel to the spatial grid, the second order no-slip boundary condition is enforced using the mid-grid bounce-back scheme (Succi, 2001).

In addition to the no-slip condition the method also allows the inclusion of wall adhesive forces (Benzi et al., 2006). The wall adhesive forces are incorporated by defining a field Ψ^{N+1} which is one at the wall nodes and zero at the fluid nodes. Including both fluid–fluid and fluid–wall interactions the total pseudo-potential force is constructed by adding $\bar\delta = N+1$ to the sum in Eq. (8).

$$\boldsymbol{F}^\delta = \frac{-1}{\Delta t}\Psi^\delta(\boldsymbol{x}) \sum_{\bar\delta=1}^{N+1} G^{\delta\bar\delta} \sum_\alpha w_\alpha \Psi^{\bar\delta}(\boldsymbol{x}+\Delta t \boldsymbol{v}_\alpha)\boldsymbol{v}_\alpha, \tag{11}$$

where for each component $\delta \in \{1,\ldots,N\}$ we have introduced a fluid–wall interaction strength $G^{\delta(N+1)}$, whose values control the contact angle. In the two-component system, the relative strength $G^{23}-G^{13}$ determines the wettability. Decreasing $G^{23}-G^{13}$ results in larger contact angle or less wettability.

In a one-component system we can specify the fluid–wall interaction with a single parameter. In that case it is instructive to use $G^{12} = G^{11}$ and specify the wall interaction by means of a wall density ρ_{wall} such that $\Psi^2 = 0$ at fluid nodes and $\Psi^2 = \Psi^1(\rho_{wall})$ at wall nodes. In doing so, there is a simple relation between ρ_{wall} and the contact angle. When $\rho_{wall} \approx \rho_{liquid}$, the wall is hydrophilic resulting in a small contact angle, and $\rho_{wall} \approx \rho_{gas}$ represents a hydrophobic wall which corresponds to a large contact angle.

3. Result and discussion

Unless stated otherwise, all results will be presented in units of ρ_0, Δx and Δt.

3.1. Validation

Before discussing the segmented flow we first study the performance of the method to deal with curved gas–liquid interfaces by considering a test case of a static liquid droplet embedded in a gas. The purpose of this preliminary study is to obtain the relations between the reduced temperature T_R (parameter a in the Carnahan–Starling EOS, Eq. (10)) and the density ratio D, the surface tension σ, as well as studying the magnitude of the spurious velocities and the thickness of the gas–liquid interface. The simulations are performed using the one-component system on a two-dimensional, periodic, square domain composed of 200×200 grid-points. The initial density field was based on the equilibrium densities provided by Eq. (10). For a given T_R the corresponding values for the liquid-like and the gas-like densities were assigned to a square region in the centre of the domain and to the complementary region, respectively. After starting the simulation, the LB field evolves to a configuration corresponding to a circular liquid-like region, of density ρ_{liq} separated by a interfacial region to a gas-like region of density ρ_{gas}.

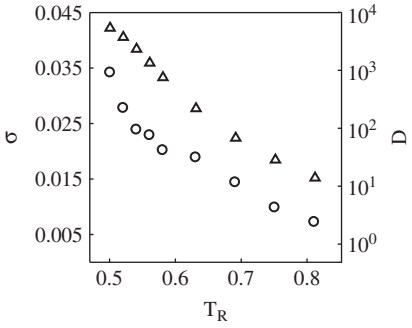

Fig. 1. Density ratio (triangles) and surface tension (circles) as a function of the reduced temperature in one-component simulations.

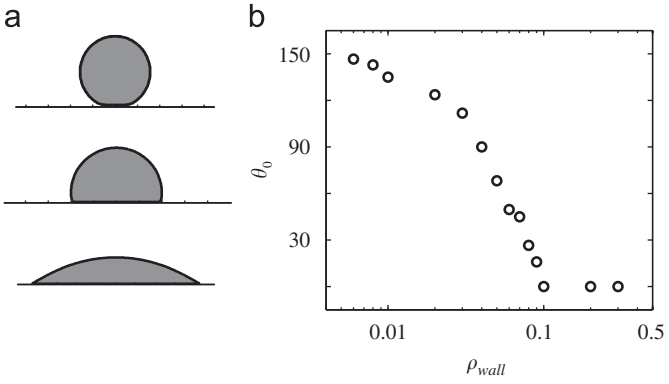

Fig. 2. (a) Droplet shapes for various fluid–wall interaction strengths. (b) Contact angle (degrees) versus wall density in one-component simulations.

As shown in Fig. 1 the density ratio D could be increased by decreasing the reduced temperature T_R. A maximum value of $D=5400$ was achieved for T_R close to 0.5. For a given T_R, surface tension σ was calculated by computing the pressure difference Δp across the gas–liquid interface as a function of the curvature $1/R$. According to the Laplace law $\Delta p = \sigma/R$, the surface tension is insensitive to the curvature $1/R$ of the interface. We have applied this procedure using several values of the reduced temperature T_R which revealed the relation between the surface tension and T_R, as shown in Fig. 1.

Although not shown, we have also applied this procedure to the two-component system, to compute the corresponding surface tension σ, and the density ratio $D = \rho_{liq}/\rho_{gas}$ for various T_R.

As explained in Section 2 the current multi-phase LB method also deals with fluid–wall interaction. In the one-component system we can compute the fluid–wall interaction by assigning a density ρ_{wall} to the wall and treating the fluid–wall interaction exactly the same as the fluid–fluid interaction. We have tested this algorithm for the case of a liquid drop attached to a solid wall. Again we have used a two-dimensional, square domain consisting of 100×100 grid-points, with a solid wall at the bottom. The problem was initialized by assigning a large liquid-like density-value inside a square region of size 20×20 which was attached to the bottom wall, and a small gas-like density-value in the remaining part.

During the simulation, the initial square droplet shape evolves into a spherical cap. The contact angle of the spherical cap θ is defined as the angle between the gas–liquid interface and the wall measured from the liquid-side of the contact point. As illustrated in Fig. 2(a), the contact angle θ varies by changing the fluid–wall interaction strength which for the one-component system is governed by the parameter ρ_{wall}. Fig. 2(b) shows the ρ_{wall}-dependence of the contact angle θ. In these figures, we have used $T_R=0.67$, corresponding to $D=130$, $\rho_{liq}=0.369$, $\rho_{gas}=0.0028$ and $\sigma=0.0160$.

3.2. Gas bubble in a partially wetting liquid in a two-dimensional channel

After these preliminary validation studies we now focus on the motion of a gas bubble in a partially wetting liquid in a two-dimensional channel. The segmented bubble is confined between two parallel solid walls which are separated by a distance of $2R$ in

Table 1
Simulation parameters.

Parameter	Run 1	Run 2	Run 3	Run 4	Run 5	Run 6	Run 7
N	1	1	1	1	1	1	2
Grid	160×32	160×32	160×32	640×128	160×32	160×32	160×32
T_R	0.67	0.67	0.67	0.67	0.75	0.81	0.65
$\rho_{liq.}$	0.369	0.369	0.369	0.369	0.3342	0.3033	0.404
ρ_{gas}	0.0028	0.0028	0.0028	0.0028	0.0117	0.0218	0.047
D	130	130	130	130	29	14	8.6
σ	0.0160	0.0160	0.0160	0.0160	0.00997	0.0074	0.0415
G^{11}	−1	−1	−1	−1	−1	−1	−1
G^{12}	−1.1	−1.3	−1.6	−1.6	−1.6	−1.6	0.1
G^{21}	–	–	–	–	–	–	0.1
G^{22}	–	–	–	–	–	–	0.0
G^{13}	–	–	–	–	–	–	−1.4
G^{23}							0.6
θ_0	79	58	37	37	37	37	49

the y-direction. The motion is induced by a constant pressure gradient $-dp/dx$ in the x-direction. The computational domain is bounded by walls in the y-direction and periodicity is applied in the x-direction. Except for a grid dependency study where we used 640×128 grid-points, we have used 160×32 grid-points in the x- and y-directions.

We have computed this flow using both a one-component ($N=1$) and a two-component ($N=2$) approach. In contrast to Section 3.1 where we used ρ_{wall}, we define the fluid–solid interaction by means of the interaction strengths $G^{\delta(N+1)}$, where the pseudo-potential of the solid phase Ψ^{N+1} is assumed to be one at the solid nodes and zero at the fluid nodes.

Different static contact angles were created by using different $G^{\delta(N+1)}$. Table 1 summarizes the different simulation parameters. We note that the viscosity ratio is equal to the density ratio D.

As initial conditions we assigned a gas-like density to the grid-points within a rectangular segment of $4R\times2R$ and a liquid-like density to the remaining grid-points. First the simulation was run without the pressure gradient, for the bubble to reach its static equilibrium shape corresponding to the static contact angle θ_0. A sketch of the resulting bubble shape is provided in Fig. 3(a). Without flow the contact angles at the front and the back of the bubble are equal to θ_0.

Imposing the pressure gradient results in the bubble to move. Since numerical stability requires $U<0.025\Delta x/\Delta t$, the present simulations were limited to a capillary number Ca (Eq. (2)) range of $0<Ca<0.1$, corresponding to a Reynolds number range of $0<Re<5$. Due to viscous forces, the bubble shape deforms as sketched in Fig. 3(b). The deformation is accompanied with changes in the contact angles. We are interested in the evolution of this dynamic contact angle and its dependence on Ca.

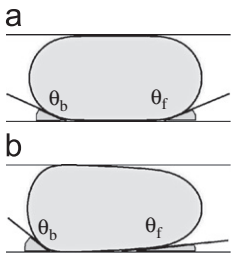

Fig. 3. Bubble shapes and dynamic contact angle in the front θ_f and the back θ_b of the bubble before (a) and after (b) applying the pressure gradient.

Fig. 4(a) shows the contact angles for both the front and the back of the bubble as functions of Ca. In agreement with the Cox–Voinov relation (Eq. (1)) our data shows a linear dependence of the deviation of the cubed contact angle $\Delta\theta^3=\theta^3-\theta_0^3$ on Ca.

The data in Fig. 4(a) correspond to one-component systems. In these simulations T_R in the Carnahan–Starling EOS (Eq. (10)) is kept constant and ρ_{wall} has been varied which lead to systems having identical surface tensions and viscosity ratios but having different static contact angles. From Fig. 4(a) it is observed that $\Delta\theta^3/Ca$ increases with θ_0. This dependence was also mentioned by Voinov (1977).

According to the Cox–Voinov equation (Eq. (1)) we can define a typical capillary number Ca^* as the inverse slope of the linear fit to the simulation data on the $(Ca,\Delta\theta^3)$-plane. The larger the Ca^*, the easier the interface moves over the wall without appreciable deformation. Conceptually Ca^* can be related to a slip length, that governs the boundary condition at the contact line.

Our goal is to study the effect of the Shan–Chen model parameters on Ca^*. For this purpose we have simulated a range of different systems, in which we have varied the density ratio between nine and 130, the grid resolution between 160×32 and 640×128 and the number of components between one and two. The parameters corresponding these different runs are summarized in Table 1.

In Fig. 4(b), we show the dynamics contact angle versus the capillary number for the different runs. The simulation results are compared to the experimental data of Hoffman (1975) which can accurately be represented by Eq. (1) using $Ca^*\approx0.01$, which is plotted by the crosses in Fig. 4(b).

Our data is in qualitative agreement with the experimental data in the sense that they follow straight lines on the $(Ca,\Delta\theta^3)$-plane. Quantitatively there are differences with the slopes being smaller than the one obtained in the experiments under almost identical conditions (compare △ to × in Fig. 4(b)). This means that the simulations over-predict Ca^*, which is equivalent to an underestimation of the amount of bubble deformation for a given flow rate.

This means that our simulated contact point moves as if there were a tremendously large slip length. Since the simulations are based on the no-slip boundary condition another mechanism is at play that allows the motion of the contact point.

Since the flow is discretized on a grid and each grid-cell corresponds to a finite volume of fluid, the contact point in the simulation is actually no point but a volume of the size of a

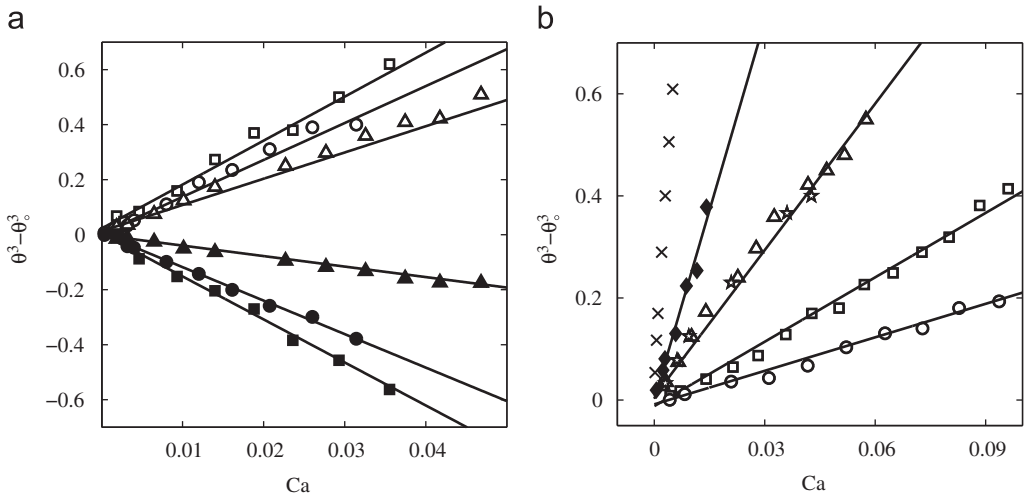

Fig. 4. (a) $\Delta\theta^3$ versus Ca for the bubble front (filled markers) and the bubble back (open markers) contact angles using one-component simulations. △, ○, □ correspond to $\theta_0=37,58,79$ respectively (Runs 1–3). (b) $\Delta\theta^3$ versus Ca for bubble back. ×, fit to experimental data for $\theta_0=37$ of Hoffman (1975). △,★,□,○, one-component simulation (Runs 3–6). ♦, two-component simulation (Run 7). Simulation parameters are given in Table 1.

grid-cell. Inside this 'contact volume' a small departure of the volume-averaged fluid velocity might be responsible for the motion of the contact point. To test this assertion we have varied the grid resolution between 160×32 and 640×128 and checked whether the simulation data showed a different slope on the $(Ca,\Delta\theta^3)$-plane. Fig. 4(b) shows that the results are nearly identical (compare △ to ★), which implies that the motion of the contact point is not due to effects of the finite discretization.

As previously mentioned, a moving contact point over a no-slip wall of a pair of truly immiscible fluids implies an infinite shear stress and is therefore not physical. In our attempt to determine the mechanism for this motion, we have ruled out finite discretization effects as a possible candidate. The only possible mechanism must be related to the miscibility of both phases, which in single component SC are composed of the same fluid, which can easily phase transition into each other. Therefore the conclusion is that the bubble is able to move due to evaporation at the front contact point and condensation at the back contact point.

In order to study the relation between phase transition and contact line motion directly would involve considering mass balances applied to a control volume surrounding the gas liquid interface. However, making accurate mass balances at the interface is an impossible task due to the spurious velocities at the interface.

Instead of using mass balances we can study the effect of phase transition on contact line motion indirectly. This is done by computing the mobility of the interface for different liquid to gas density ratio's, which correspond to different levels of evaporation and condensation at the moving contact point. By increasing the density ratio we expect a reduced amount of phase transition and therefore a reduced mobility Ca^* of the contact point. To verify this hypothesis we have conducted several one-component simulations with constant θ_0 but with decreasing values for the reduced temperature T_R. Fig. 4(b) demonstrate that decreasing T_R from 0.81 to 0.67 decreases Ca^* by a factor of two (compare △, □ and ○), which confirms our assertion that mobility of the contact point is due to phase transition.

However in these single component simulations, we have not only changed the amount of phase transition but also the viscosity ratio μ_{liq}/μ_{gas}, which is identical to the density ratio in our LB simulations. The viscosity ratio is known to have a significant effect on the dynamic contact angle (Cox, 1986a).

In order to separate the effect of the viscosity ratio from the effect of the phase transition, we will now compare a single component system with a two-component system, which have roughly the same viscosity ratio but marked different levels of immiscibility. Since each phase is represented by a different component with a very high degree ($>99\%$) of purity, the two-component system has a much larger immiscibility as compared to the one-component system. The two-component system (♦) has a density ratio of nine and is compared to a one-component system having a density ratio of 14 (○) in Fig. 4(b). The two-component system predicts a smaller Ca^* by a factor of three, even though it corresponds to a smaller density ratio. This result confirms that phase transition is the mechanism that allows the contact point to move over a no-slip wall in the Shan–Chen model. Controlling phase transition by increasing the density ratio or by using two instead of one components reduces the mobility of the contact point to values closer to the experimental data of Hoffman (1975).

4. Summary and conclusion

Both the single component and the two-component Shan–Chen models were used to simulate the contact angle θ of a moving gas bubble in a partially wetting liquid in a two-dimensional channel. In agreement with the well-established Cox–Voinov equation (Eq. (1)) we found a linear dependence of $\Delta\theta^3=\theta^3-\theta_0^3$ on the capillary number Ca. The slope on the $(Ca,\Delta\theta^3)$-plane, however, was smaller than that observed in the experiments of Hoffman (1975). A smaller slope corresponds to a larger mobility of the contact point. This is counterintuitive since the simulations are based on no-slip boundary conditions, while in reality a moving contact point requires the fluid to slip over the wall.

We investigated the source of this discrepancy. By eliminating the finiteness of the discretization as a possible candidate, we concluded that the mobility of the contact point is due to phase transition at the interface. In support of this we found that the mobility of the contact point could be reduced to more realistic values by increasing the immiscibility of the fluids. This can be done by (i) increasing the density ratio in the one-component system and by (ii) switching to the more immiscible two-component system.

Acknowledgement

This research is supported by the Dutch Technology Foundation STW, the Applied Science Division of the Netherlands Organization for Scientific Research (NWO).

References

Aidun, C.K., Clausen, J.R., 2010. Lattice Boltzmann method for complex flows. Annual Review of Fluid Mechanics 42, 439–472.
Akker, H.E.A., 2006. The details of turbulent mixing process and their simulation. Advances in Chemical Engineering 31, 151–229.
Benzi, R., Biferale, L., Sbragaglia, M., Succi, S., Toschi, F., 2006. Mesoscopic modeling of a two-phase flow in the presence of boundaries: the contact angle. Physical Review E 74.
Briant, A.J., Wagner, A.J., Yeomans, J.M., 2004. Lattice Boltzmann simulations of contact line motion. I. Liquid–gas systems. Physical Review E 69, 031602-1–031602-14.
Carnahan, N.F., Starling, K.E., 1970a. Analytical equation for rigid spheres: application to the model of Longuet–Higgins and Widom for the melting of argon. Physical Review A 1, 1672–1673.
Carnahan, N.F., Starling, K.E., 1970b. Thermodynamic properties of a rigid-sphere fluid. Journal of Chemical Physics 53, 600–603.
Cox, R.G., 1986a. Dynamics of the spreading of liquids on a solid surface. Part 1. Viscous flow. Journal of Fluid Mechanics 168, 169–194.
Cox, R.G., 1986b. Dynamics of the spreading of liquids on a solid surface. Part 2. Surfactants. Journal of Fluid Mechanics 168, 195–220.
Fan, L., Fang, H., Lin, Z., 2001. Simulation of contact line dynamics in a two-dimensional capillary tube by the lattice Boltzmann model. Physical Review E 63, 516031–516036.
Grubert, D., Yeomans, J.M., 1999. Mesoscale modeling of contact line dynamics. Computer Physics Communications 121, 236–239.
Harting, J., Kunert, C., Hyväluoma, J., 2010. Lattice Boltzmann simulations in microfluidics: Probing the no-slip boundary condition in hydrophobic, rough, and surface nanobubble laden microchannels. Microfluidics and Nanofluidics 8, 1–10.
Hoffman, R.L., 1975. A study of the advancing interface. I. Interface shape in liquid–gas systems. Journal of Colloid and Interface Science 50, 228–241.
Hyväluoma, J., Koponen, A., Raiskinmäki, P., Timonen, J., 2007. Droplets on inclined rough surfaces. European Physical Journal E 23, 289–293.
Jiang, T.-S., Soo-Gun, O.H., Slattery, J.C., 1979. Correlation for dynamic contact angle. Journal of Colloid and Interface Science 69, 74–77.
Koplik, J., Banavar, J.R., Willemsen, J.F., 1988. Molecular dynamics of Poiseuille flow and moving contact lines. Physical Review Letters 60, 1282–1285.
Koplik, J., Banavar, J.R., Willemsen, J.F., 1989. Molecular dynamics of fluid flow at solid surfaces. Physics of Fluids A 1, 781–794.
Lerou, J.J., Ng, K.M., 1996. Chemical reaction engineering: a multiscale approach to a multiobjective task. Chemical Engineering Science 51, 1595–1614.
Lunkad, S.F., Buwa, V.V., Nigam, K.D.P., 2007. Numerical simulations of drop impact and spreading on horizontal and inclined surfaces. Chemical Engineering Science 62, 7214–7224.
Raabe, D., 2004. Overview of the lattice Boltzmann method for nano- and microscale fluid dynamics in materials science and engineering. Modelling and Simulation in Materials Science and Engineering 12, R13–R46.
Ralston, J., Popescu, M., Sedev, R., 2008. Dynamics of wetting from an experimental point of view. Annual Review of Materials Research 38, 23–43.

Sbragaglia, M., Sugiyama, K., Biferale, L., 2008. Wetting failure and contact line dynamics in a Couette flow. Journal of Fluid Mechanics 614, 471–493.
Shan, X., 2006. Analysis and reduction of the spurious current in a class of multiphase lattice Boltzmann models. Physical Review E 73, 1–4.
Shan, X., Chen, H., 1993. Lattice Boltzmann model for simulating flows with multiple phases and components. Physical Review E 47, 1815–1819.
Sheng, P., Zhou, M., 1992. Immiscible-fluid displacement: contact-line dynamics and the velocity-dependent capillary pressure. Physical Reviews A 45, 5694–5708.
Spelt, D.M., 2005. A level-set approach for simulations of flows with multiple moving contact lines with hysteresis. Journal of Computational Physics 207, 389–404.
Succi, S., 2001. The Lattice Boltzmann Equation for Fluid Dynamics and Beyond. Oxford University Press, New York.
Tsamatsoulis, D.C., Papayannakos, N.G., 1996. Partial wetting of cylindrical catalytic carriers in trickle-bed reactors. AICHE Journal 42, 1853–1863.
Van Den Akker, H.E.A., 2010. Toward a truly multiscale computational strategy for simulating turbulent two-phase flow processes. Industrial and Engineering Chemistry Research 49, 10780–10797.
Vervloet, D., Kamali, M.R., Gillissen, J.J.J., et al., 2009. Intensification of co-current gas–liquid reactors using structured catalytic packings: a multiscale approach. Catalysis Today 147, S138–S143.
Voinov, O.V., 1977. Hydrodynamics of wetting. Fluid Dynamics 11, 714–721.
Yuan, P., Schaefer, L., 2006. Equations of state in a lattice Boltzmann model. Physics of Fluids 18.
Zhang, J., 2011. Lattice Boltzmann method for microfluidics: models and applications. Microfluidics and Nanofluidics 10, 1–28.